RSC Advances

PAPER

View Article Online
View Journal | View Issue

Cite this: *RSC Adv.*, 2023, **13**, 11762

Influence of high altitude on the strength of aerated concrete

Biwen Liu,[a] Qian Zhang,[b] Yuxiang Zhao,[a] Dongdong Huan[a] and Xinzhong Liu*[a]

Aerated concrete specimens were prepared at Fuzhou and Lhasa with the same processing conditions. The compressive strengths of the specimens in Lhasa were lower than that in Fuzhou. We used SEM-EDS, XRD, FT-IR and MIP to study their microstructure in order to find the reasons made for differences in strength. Furthermore, the effect of the preparation process on the material strength was analyzed. The results showed that a low ambient temperature affected the autoclave curing process of the aerated concrete. A longer time was needed to reach the desired constant temperature, resulting in an insufficient degree of hydration, a low level of tobermorite generation, poor crystallinity, high porosity, an uneven pore size distribution, more harmful pore content above 200 nm and unsatisfactory strength. Under low environmental pressure, increasing autoclave pressure can promote the better formation of tobermorite to improve the strength of aerated concrete.

Received 14th October 2022
Accepted 1st April 2023

DOI: 10.1039/d2ra06498g

rsc.li/rsc-advances

Introduction

Different autoclaved curing systems (*i.e.*, raw materials, autoclave time, pressure, temperature) affect the hydration products and pore structures of aerated concrete. The pore structure,[1,2] contents of the hydration products and relative crystallinity[3] play decisive roles in determining the mechanical properties of the aerated concrete. Due to the limited synchronization of tobermorite formation, the pore wall structure is obviously stratified. The layer composed of tobermorite converts the pores into hollow rigid spheres and plays the role of the skeleton that supports the "aggregate".[4] The tobermorite phase is the main crystalline phase providing strength development of the aerated concrete. Tobermorite with higher crystallinity aids in the formation of a dense microstructure. The C–S–H gel generated and the highly crystalline layered tobermorite formed in the hydrothermal synthesis interlaced to form a dense network structure and increase the strength of the aerated concrete.[5–7]

Various factors, such as the types and ratios of the raw materials,[8–10] autoclave temperature and time,[11–13] greatly affect the formation of hydration products by the aerated concrete. Li *et al.*[14] changed the pore structure and surface characteristics of the product by adding additives during autoclave curing, enhanced the formation of tobermorite, and thus improved the compressive strength of the AAC. Quartz sand with the appropriate fineness reacts well in a short time to form tobermorite with high crystallinity. By using waste sugar slag or BOF instead of lime,[3,15] the aerated concrete generated a higher proportion of the tobermorite phase. Its structural surface showed a finer needle-like crystal morphology and a higher crystallinity.

To prepare aerated concrete that can adapt more effectively to this environment, we used the same process to prepare aerated concrete samples at high and low altitudes, compared their strength differences, and analyzed the possible reasons for the differences by determining the composition and microstructures of their hydration products. By comparing the strengths of aerated concrete samples prepared under different autoclave pressures in the plateau area, the hydration products and pore structure were analyzed, and the effect of the autoclaved curing process on strength was explored. The differences in the climates for high and low altitudes are mainly the temperatures and pressures, and the effect of autoclave pressure on strength was greater than that of the autoclave time. Therefore, we studied the mechanism for the effect of autoclave pressure on intensity.

Materials and methods

Raw materials

The sand tailings used in this study were obtained from an aerated concrete plant in Lhasa. The consistency of the cement was 27.20%. The solid content of the water-based aluminum powder paste was 65%, and the active rate of the solid content was 92%. The physical properties and chemical analysis of the main materials are listed in Table 1. The digestion curve of quicklime is shown in Fig. 1.

Preparation of specimens

The samples were prepared by using the ratio of raw sand materials to prepare B05-grade aerated concrete. Several raw

[a]Fujian University of Technology, China. E-mail: liuxinzh01@163.com
[b]Fuzhou University, China

Table 1 Physical and chemical compositions of materials

	Sand tailings	Lime	Cement	Plaster
Consistency, %	—	—	27.20	—
Loss of ignition, %	5.89	0.22	3.13	13.56
SiO_2, %	71.49	5.66	24.98	6.18
Al_2O_3, %	12.21	1.78	3.73	0.97
CaO, %	3.12	69.55	58.92	32.45
MgO, %	4.25	3.21	3.86	1.78
Fe_2O_3, %	2.74	0.64	2.64	0.38
SO_4^{2-}, %	—	—	—	44.34

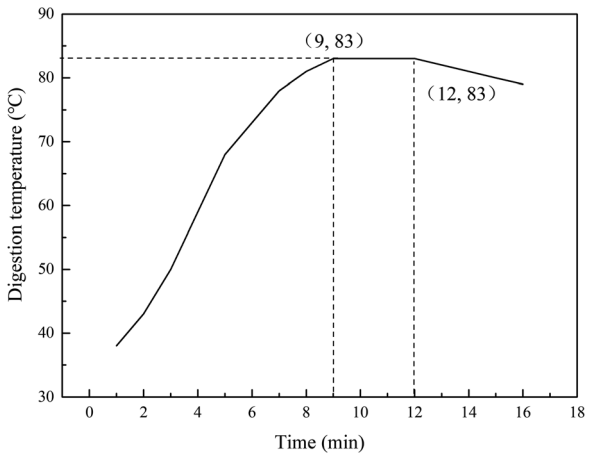

Fig. 1 Digestion curve of quicklime.

materials were added to the wet mill according to the ratio of sand tailings : lime : cement : gypsum = 63 : 19 : 17 : 2 for grinding and pulping. The water-based aluminum powder paste (0.074%) was measured and poured into the mixer and formed into a slurry. The slurry temperature met the process requirements before pouring. Then, the green body was placed in a static room at a temperature of approximately 43 °C for 2.0–3.0 hours. After the green body reached the cutting strength, it was transported to the pouring–precuring–cutting cycle line and cut. The green body was then placed into the autoclave and cured, completely cured after 28 days. Then, the desired sample was obtained (Table 2 and Fig. 2).

Test methods and processes

Four different cubic specimens (the length of each edge was 3.94 in [100 mm]) were investigated. The variables included vapor pressure and external ambient pressure.

The dry density and compressive strength of air-entrained concrete can be determined by means of formula (2) and (3), respectively:

$$r_0 = \frac{M_0}{V} \times 10^6 \quad (1)$$

$$W_s = \frac{M - M_0}{M} \times 100\% \quad (2)$$

where r_0 (kg m^{-3}) is the dry density of the specimen, M_0 (g) is the weight after drying, V (mm^3) is the volume of the specimen, W_s is the mass moisture content of the specimen, and M (g) is the weight before drying of the specimen.

$$f_{cc} = \frac{p_1}{A_1} \quad (3)$$

where f_{cc} (MPa) is the compressive strength of autoclaved concrete, p_1 (N) is the failure load of the specimen, and A_1 (mm^2) is the pressurized area.

After the compressive strength test was completed, the crushed samples was made into cubes (the length of each edge was 5 mm). The surface of the samples were polished and sprayed with gold before the samples was characterized with a Czech TESCAN MIRA LMS field emission scanning electron microscope. The settings for the SEM analyses included an acceleration voltage of 5 keV, and the secondary electron image mode was used. Then, dotting the energy spectrum at the location where the lamellar structure appeared through SEM.

Other broken samples remaining after the compressive strength tests were ground into powders. Then, the microstructures of these sample powders was investigated by XRD and FT-IR analyses to elucidate the influence of the preparation process on the material strengths.

The crystal phase compositions and proportions of the prepared samples were analyzed with a Japanese Ultima IV X-ray diffractometer. The settings for the XRD analyses included a Cu radiation source. The samples were scanned over a 2θ range 5 to

Table 2 Comparison of process parameters of different specimens

Samples	Ratio of raw materials	Autoclave system	Place
A	Sand tailings : lime : cement : plaster = 63 : 19 : 17 : 2 Aluminum powder paste: 0.074% Ratio of water to material: 0.6–0.65	Autoclave pressure: 1.2 MPa Autoclave temperature: 190 °C Autoclave time: 8 h	Fuzhou
B	Sand tailings : lime : cement : plaster = 63 : 19 : 17 : 2 Aluminum powder paste: 0.074% Ratio of water to material: 0.6–0.65	Autoclave pressure: 1.2 MPa Autoclave temperature: 190 °C Autoclave time: 8 h	Lhasa
C	Sand tailings : lime : cement : plaster = 63 : 19 : 17 : 2 Aluminum powder paste: 0.074% Ratio of water to material: 0.6–0.65	Autoclave pressure: 1.25 MPa Autoclave temperature: 192 °C Autoclave time: 8 h	Lhasa
D	Sand tailings : lime : cement : plaster = 63 : 19 : 17 : 2 Aluminum powder paste: 0.074% Ratio of water to material: 0.6–0.65	Autoclave pressure: 1.3 MPa Autoclave temperature: 194 °C Autoclave time: 8 h	Lhasa

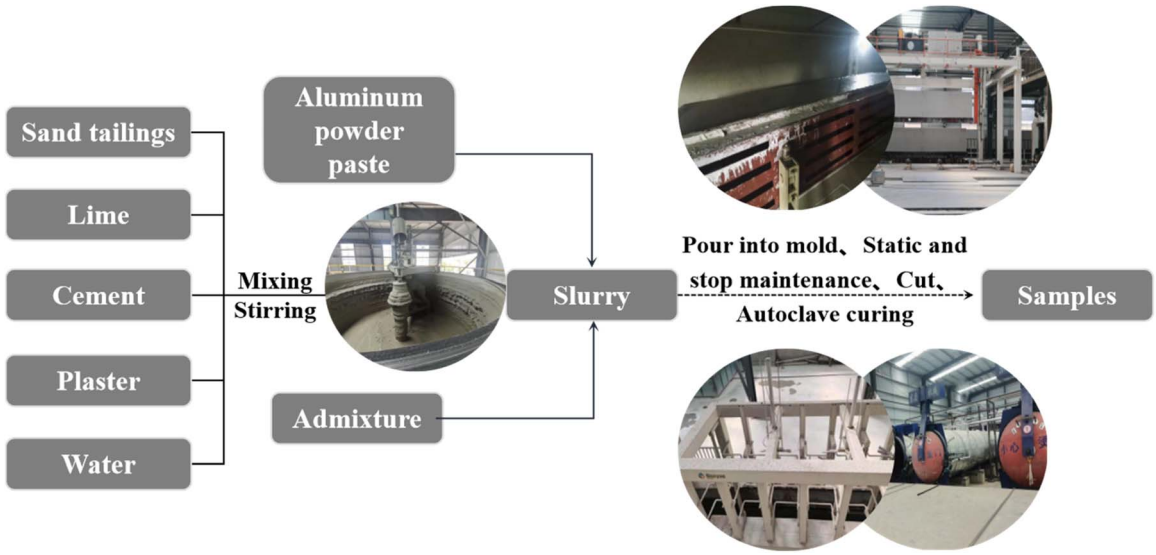

Fig. 2 Process flow chart of autoclaved concrete.

80° with a step size of 0.02°. During the measurements, XRD experiments were performed at 40 kV and 15 mA.

The crystal plane distance was calculated with the Bragg equation:

$$2d \sin \theta = n\lambda \quad (4)$$

where d (nm) is the distance between the crystal planes, n (=1) is the expression for the first-order diffraction, λ (nm) is the X-ray wavelength (0.154 056 nm), and θ is the diffraction angle.

The functional groups of the sample were characterized with a Bruker ALPHA Fourier transform infrared spectrometer. With potassium bromide as the background, potassium bromide and the sample powder were mixed, ground and pressed, and the wavenumber scanning range was 400–4000 cm^{-1}.

Using the crushed sample from the previous compressive strength test and cutting them into cubes (the length of each edge was 10 mm). We used high-performance automatic mercury porosimeter (American Micromeritics AutoPore V 9620) to test the porosities and pore size distributions of the samples. And the pore size range was 0.003–1000 μm.

Results and discussion

Compressive strength

According to GB/T11968-2020 and Table 3, the strength grade of the products in Group A and Group D reached A5.0, whereas that of the products in Group B and Group C only reached A3.5. This is due to the low-temperature and low-pressure environment of the plateau during the production of Group B products, and it was difficult to achieve the ideal autoclave temperature during the production process. As a result, the same process was used for Groups A and B, but the strength of the prepared samples was quite different. As the autoclave pressure increased, the compressive strength of the samples increased. When the autoclave pressure reached 1.3 MPa and the autoclave temperature reached 194 °C (Group D), the strength of the samples was equal to that of the samples prepared in Fuzhou (Group A).

The effect of different autoclave pressures on the microstructure

Fig. 3 shows the SEM images of different samples. Regular flaky crystals, which are tobermorite, can be clearly seen in the picture. The surrounding white flocculent materials are semi-crystalline C–S–H gels. The tobermorite crystals and C–S–H gels are interspersed to form a whole, forming a tight mesh structure to provide strength to aerated concrete.[16] Pores were observed between adjacent tobermorite crystals. Moreover, the structure is relatively loose, indicating that sample B has a lower tobermorite content. Thus, its compressive strength was relatively low. Even though sample B and sample A were prepared under the same process conditions, there are still large differences in

Table 3 Comparison of the compressive strengths of different samples after autoclave curing for 8 hours

Samples	Shape	Size	Dry density (r_0/kg m^{-3})	Compressive strength at 28 days (f_{cc}/MPa)	GB/T11968-2020 Strength level	Actual strength level
A	Cube	100 mm × 100 mm × 100 mm	714	5.2	$f_{cc} \geq 2.0$ MPa, A2.0	A5.0
B	Cube	100 mm × 100 mm × 100 mm	605	4.1	$f_{cc} \geq 2.5$ MPa, A2.5	A3.5
C	Cube	100 mm × 100 mm × 100 mm	612	4.3	$f_{cc} \geq 3.5$ MPa, A3.5	A3.5
D	Cube	100 mm × 100 mm × 100 mm	710	5.1	$f_{cc} \geq 5.0$ MPa, A5.0	A5.0

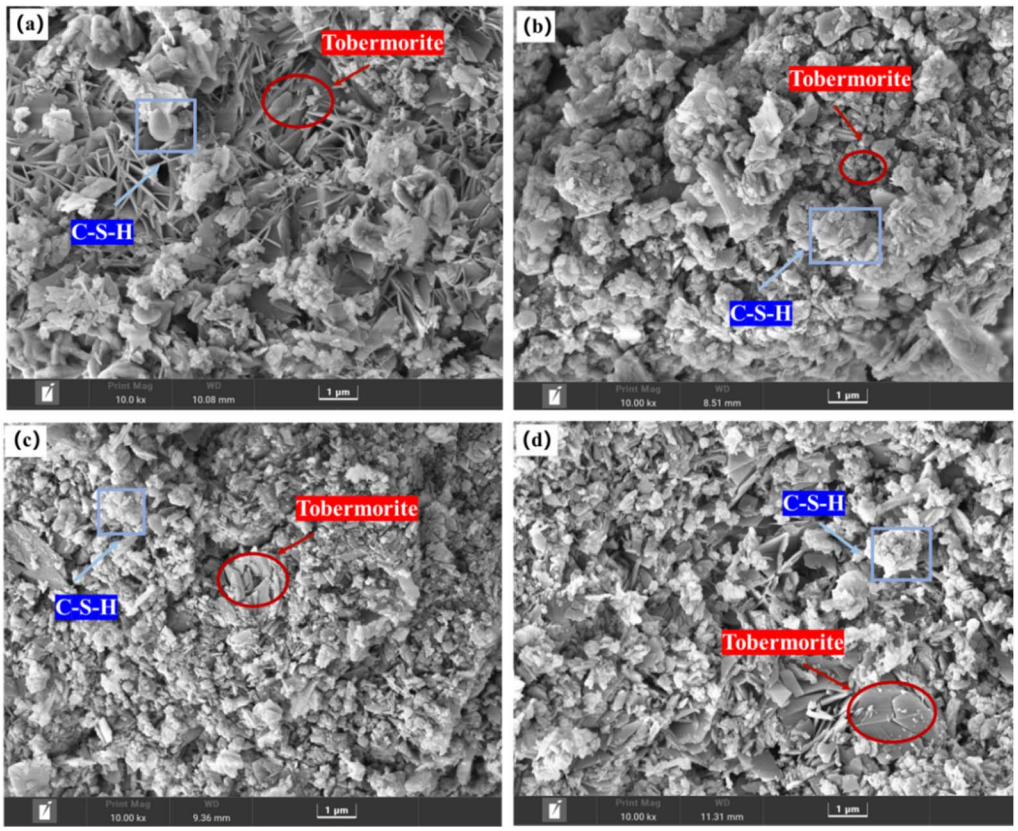

Fig. 3 SEM images of the samples. (a) Sample A; (b) sample B; (c) sample C; (d) sample D.

strength between these samples. This may be due to the difference in the external environment; sample B required a longer time to reach a constant temperature. Hence, the degree of hydration was not enough, the amount of tobermorite generated was small, and the crystallinity was not good at the same autoclave time.

Additionally, with an increase in the autoclave temperature, the content of tobermorite in the test block increased, and the bond between the hydration products became tighter. It was evident that the content of tobermorite in sample D was equivalent to that in sample A, while the distribution of tobermorite crystals in sample A was more regular and orderly. Therefore, the strength of sample A was slightly higher than that of sample D.

To explore the element differences of the hydration products generated under different autoclave curing conditions, a random point was selected in the leaf-shaped area (*i.e.*, tobermorite) for EDS detection. From Fig. 4 and Table 4, we can see that C, O, Ca, Si and Al were detected in tobermorite in the samples, but the contents of Ca and Si were different, which may be due to different autoclave curing conditions, resulting in different crystal forms of the tobermorite, which affected the final strength of the product. The Al contents were also different, which may have been due to different temperatures in the autoclave, which would lead to different participation of the active-Al_2O_3 in the hydrothermal reaction.

The effect of different autoclave pressures on the hydration products

Fig. 5 shows the XRD spectra of different samples. The hydration products of each sample were basically the same, mainly including tobermorite, C–S–H gel, hydrated garnet and some SiO_2, which was not involved in the hydration reaction of the C–S–H gel. In particular, tobermorite and C–S–H gel were the main contributors to the strength. In the initial constant-temperature stage of autoclave curing, a large number of C–S–H gels were generated. At the same time, hydrated calcium aluminate reacted with SiO_2 to generate hydrogarnet. With the continuous progress of the reaction, the crystallinity of the calcium silicate hydrate continued to increase, and tobermorite appeared.[17]

The crystalline state of tobermorite greatly affected the aerated concrete. MDI-Jade software was used to calculate the corresponding half-height width and peak intensity of the tobermorite phase (T) with different X-diffraction d values. The difference between the full width at half maximum and the peak intensity was used to characterize the difference in the phases, and then the macroscopic properties were determined. The calculation results are shown in Table 5.

The crystallinity of the tobermorite was calculated with formula (5):[18]

$$\text{Relative crystallinity} = \frac{I_{(002)}}{I_{(220)}} \quad (5)$$

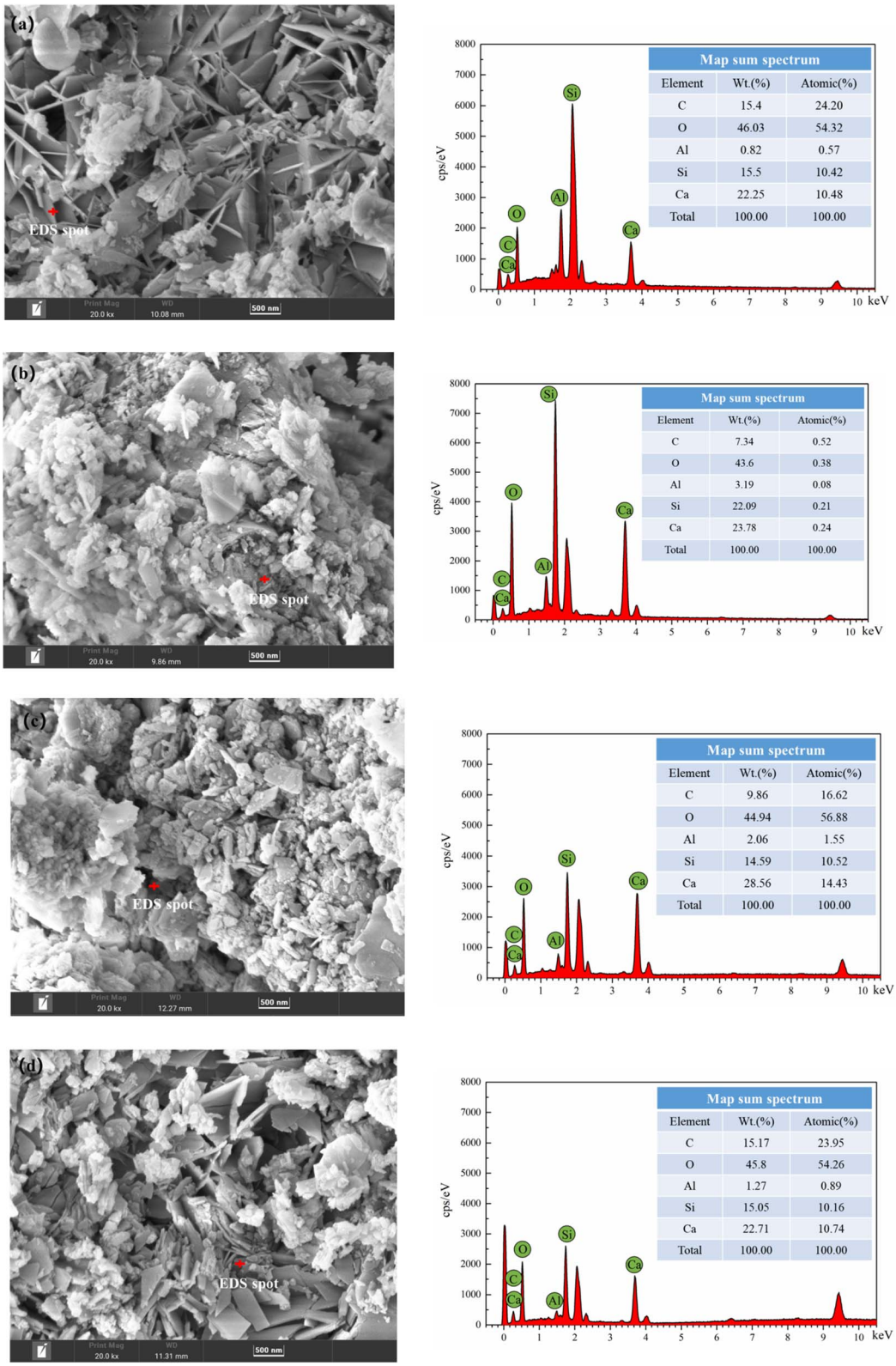

Fig. 4 EDS spectra of tobermorite in different autoclaved aerated concretes; (a) sample A; (b) sample B; (c) sample C and (d) sample D.

where $I_{(002)}$ and $I_{(220)}$ are the diffraction peak sizes on the (002) and (220) crystal planes, respectively.

After this calculation, the relative crystallinities of test pieces A, B, C and D tobermorite were 0.35, 0.24, 0.26 and 0.33, respectively. Test block A had higher crystallinity and a better crystalline state, so the strength of A was greater, consistent with the previous results of compressive strength.

Table 4 Contents of the elements in the tobermorite samples

Samples	C (wt/%)	O (wt/%)	Al (wt/%)	Si (wt/%)	Ca (wt/%)
A	15.4	46.03	0.82	15.5	22.25
B	7.34	43.6	3.19	22.09	23.78
C	9.86	44.94	2.06	14.59	28.56
D	15.17	45.8	1.27	15.05	22.71

The presence of hydrated garnet inhibited the formation of tobermorite and eventually led to insufficient strength of the test block. According to JCPDS No. 38-0368, the diffraction peaks at $2\theta = 28°$ correspond to the (400) crystal planes, and the diffraction peak intensity for hydrated garnet was the most obvious of the samples. Fig. 3 and Table 6 show that the diffraction peak intensity for hydrogarnet near $2\theta = 28°$ decreased in the order B > C > D > A, so many substances had adverse effects on the compressive strengths in sample B and sample C, and the intensities were less than those of sample A and sample D.

Excessive residual quartz in the test block affected the formation of tobermorite in the solidified body, loosening the structure of tobermorite and resulting in a decrease in the strength of the test piece.[19] The diffraction peaks at 20.8°, 26.6°, 39.4°, 42.4°, 60.0° and 68.2° corresponded to the (100), (101), (102), (200), (211) and (301) crystal planes of SiO_2, respectively, which matched the standard card JCPDS No. 45-1480. The intensity of the quartz diffraction peak at 26.6° was the strongest. Table 7 shows that the diffraction peak intensity of quartz sand at $\theta = 26.6°$ decreased as B > C > D > A. Therefore, samples B, C, and D had many substances with adverse effects on the compressive strength, and the strength of sample A was greater than that of the other three.

Effects of different autoclave pressures on functional groups

The polymerization state of the $[SiO_4]^{4-}$ tetrahedron in the aerated concrete samples and characterization of other related functional groups are shown in Fig. 6. The FTIR spectra of the four samples were basically consistent. The most intense

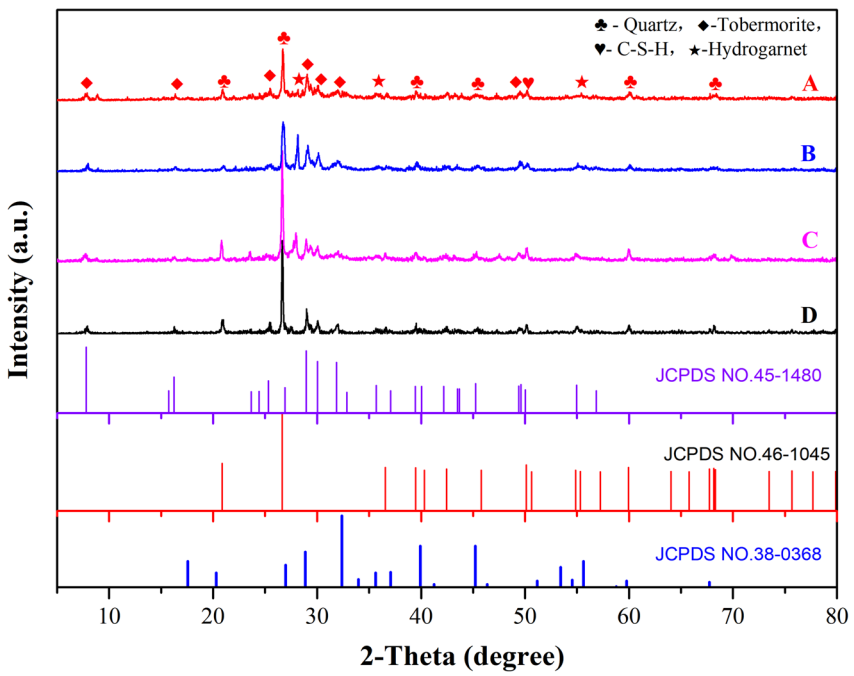

Fig. 5 XRD patterns of different aerated concrete samples.

Table 5 FWHM and peak intensity for tobermorite in the different samples

		A		B		C		D	
Crystal surface	*d*	FWHM	Peak intensity	FWHM	Peak intensity	FWHM	Peak intensity	FWHM	Peak intensity
(002)	1.133	0.286	14	0.333	14	0.194	11	0.250	14
(201)	0.548	0.153	9	0.291	9	0.195	9	0.179	9
(205)	0.350	0.224	20	0.312	9	0.377	11	0.266	22
(220)	0.308	0.172	40	0.134	51	0.182	41	0.160	42
(222)	0.298	0.203	26	0.240	26	0.238	32	0.221	30
(008)	0.282	0.299	15	0.245	15	0.221	11	0.264	22
(425)	0.200	0.264	11	0.246	11	0.215	8	0.317	14
(2,2,10)	0.182	0.192	29	0.218	27	0.285	21	0.172	25

Table 6 FWHM and peak intensity for different samples of hydrogarnet

		A		B		C		D	
Crystal surface	*d*	FWHM	Peak intensity	FWHM	Peak intensity	FWHM	Peak intensity	FWHM	Peak intensity
(400)	0.318	0.135	26	0.178	53	0.182	41	0.189	32

Table 7 FWHM and peak intensities for different samples of quartz sand

		A		B		C		D	
Crystal surface	*d*	FWHM	Peak intensity	FWHM	Peak intensity	FWHM	Peak intensity	FWHM	Peak intensity
(101)	0.230	0.119	103	0.232	279	0.134	234	0.126	134

vibrational peak was observed near 965 cm^{-1}, which was attributed to the asymmetric stretching vibration of the Si–O–Si bond. The characteristic peaks appearing near 451 cm^{-1} and 673 cm^{-1} were attributed to the deformation vibration and the bending vibration of the O–Si–O bond, respectively, which are the characteristic spectral lines of tobermorite.[20–22] It is obvious from the figure that the asymmetric stretching vibration band of Si–O–Si in the hydration product of sample A shifted to a higher wavenumber than those of the hydration products of the other samples. This shows that the polymerization degree of the silicate anion in the hydration product was higher than that in the other test pieces and that the hydration degree was higher.[23,24] Hence, the compressive strength was also relatively high. In addition, the spectral band at 598 cm^{-1} may have arisen from a breathing vibration of the Si–O–Si bonds. As the degree of polymerization of the silicon–oxygen bonds in sample A was higher than those of the other samples, sample A had a peak where the others had no obvious peak.

Owing to the presence of some crystal water in tobermorite, the peaks near 3448 cm^{-1} and 1622 cm^{-1} were attributed to the asymmetric stretching vibration and bending vibration of OH^-.[25] The main reason for the appearance of crystal water is that even if the reaction occurred under high-temperature conditions, the crystal water present in the hydrated product completely evaporated.

Moreover, the peaks at 1464 cm^{-1} and 875 cm^{-1} correspond to the asymmetric stretching vibration and the flexural vibration absorption of CO_3^{2-}.[26–28] In addition, the characteristic

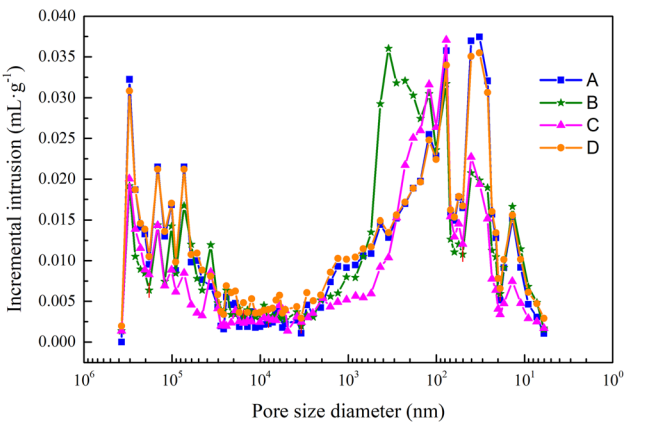

Fig. 7 Pore size distribution diagrams for different aerated concrete samples.

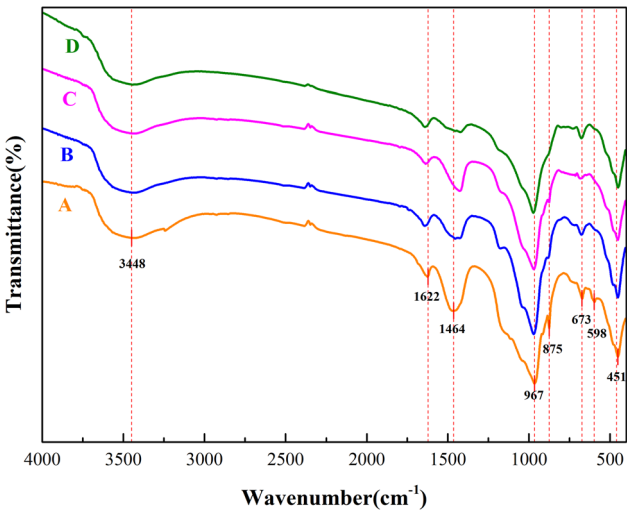

Fig. 6 FTIR curves of different aerated concrete samples.

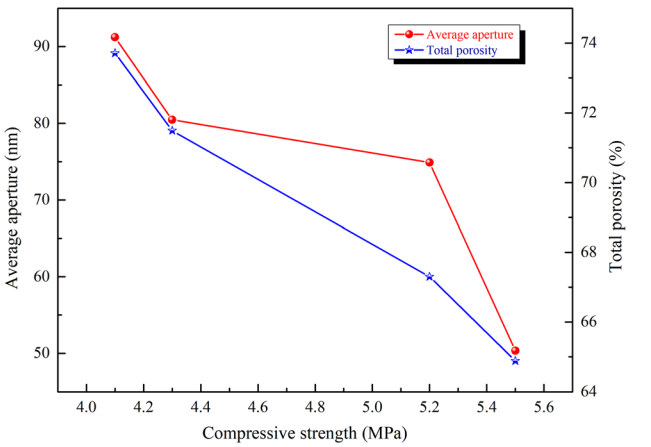

Fig. 8 Relationships between the compressive strength, porosity and average pore size.

Table 8 Results of the mercury intrusion tests

Samples	Total porosity	Average aperture (nm)	Aperture distribution				
			<20 nm	20–50 nm	50–200 nm	200 nm–1 μm	>1 μm
A	64.88%	50.33	15.5%	14.3%	27.9%	11.5%	30.8%
B	73.71%	91.21	5.5%	10.8%	22.6%	21.9%	39.2%
C	71.49%	80.46	4.1%	14.9%	33.5%	12.4%	35.1%
D	67.30%	74.88	14.2%	18.9%	22.3%	11.8%	32.8%

diffraction peaks of calcite were detected in the XRD spectrum. This may be the reason for the adsorption of a small amount of CO_3^{2-} in the hydrated silicate or the small amount of carbonaceous material formed during the production process. The asymmetric stretching vibration absorption peak intensity of CO_3^{2-} of sample D in the figure was smaller than that of the other samples, indicating that its carbonization degree was the smallest. On the other hand, the characteristic peak intensity of Si–O–Si was smaller than that of sample A, so the strength of sample A was slightly larger than that of sample D and higher than that of samples B and C. This result is in line with the previous test results of compressive strength.

The effect of different autoclave pressures on the aperture distribution

The pore size has a significant impact on the strength of the aerated concrete. Aerated concrete with large pores will also have a lower strength. A aperture diameter greater than 0.2 μm indicates multihazard holes.[29] According to the mercury intrusion test results, the proportions of samples A, B, C and D with pore sizes greater than 200 nm were 42.3%, 61.1%, 47.5% and 44.6%, respectively. The pore size distribution of sample B was greater than 200 nm, which was the largest among the four samples, indicating that sample B had the highest multihole content. In addition, Fig. 7 shows that the pore sizes of sample B had a large distribution in various ranges, and the pore structure was not uniformly distributed, which had a negative effect on the strength. This may have been due to the insufficient hydration reaction caused by the low autoclave pressure; the gaps between the pores were not filled, the pore gaps increased, and the strength decreased.

The average pore size reflected the average value of the internal pore size in the aerated concrete block. The larger the average pore size was, the more obvious the coalescence of bubbles. As the amount of aluminum powder was increased, the distances between particles decreased. When the aluminum powder particles were gradually transformed into expanded bubbles, the distances between bubbles decreased, that is, the porosity decreased, and the bubbles floated upward during the expansion process, which increased the probability of coalescence between bubbles and formation of larger bubble diameters.

Fig. 8 shows that the porosity, average pore size and compressive strength were inversely proportional. According to Table 8, with an increase in the autoclave pressure from 1.2 MPa to 1.3 MPa, the total porosity of the sample decreased from 73.71% to 67.30%, the average pore size decreased from 91.21 nm to 74.88 nm, and the compressive strength increased from 4.1 MPa to 5.1 MPa. As the autoclave temperature rose and the hydration reaction continued, more hydration products were formed, the gaps between the pores were filled, and the hydration products were wrapped and crossed to form a dense spatial network structure, thus refining the original pore distribution. The reduction of average pore size and porosity made the compressive strength develop in a favorable direction.

Conclusions

To achieve the same strength of autoclave-aerated concrete, the autoclave curing process used in the plateau and low-altitude areas was 1.3 MPa, 194 °C and 1.2 MPa, 190 °C, respectively. A low ambient temperature will make it take longer to reach the corresponding constant temperature. Otherwise, the degree of hydration is not enough, the amount of tobermorite generated is small, and the crystallinity is not good, which will cause unsatisfactory strength. With increasing autoclave pressure, the degree of hydration deepens. The content and crystallinity of tobermorite also increase. Hence, the compressive strength is enhanced. In addition, formation of the hydration products was increased to continuously fill the pores, thus forming a more compact network structure and improving the compressive strength of the sample.

With increasing autoclave pressure, the hydration reaction continued, the yield of the hydration products increased, the gaps between the pores were filled, and the hydration products were wrapped and crossed to form a dense spatial network structure, thus refining the original pore distribution and increasing the compressive strength.

This paper was focused on the strength difference of aerated concretes formed in high and low-altitude areas. Due to the limited time, the durability was not studied. To enable the application of aerated concrete in building walls in cold and high-altitude areas and provide a theoretical basis for the design and construction of local building materials, tests of the split pressure ratios and durabilities (dry shrinkage, carbonization, freeze–thaw cycle, ultraviolet aging, *etc.*) of aerated concretes will be carried out in future work.

Author contributions

Formal analysis and writing—review and editing, B. Liu; writing—original draft preparation, writing—review and

editing, and funding acquisition, Q. Zhang and D. Huang; investigation, Y. Zhao; resources, formal analysis, and investigation, X. Liu. All authors have read and agreed to the published version of the manuscript.

Conflicts of interest

The authors declare that there are no conflicts.

Acknowledgements

The authors gratefully acknowledge the support received from National Key Research and Development Program (Grand No. 2019YFC1904103).

References

1 G. Chen, F. Li, J. Geng, P. Jing and Z. Si, *Constr. Build. Mater.*, 2021, **294**, 123572.
2 J. Fu and Y. Yu, *Adv. Civ. Eng.*, 2019, **2019**, 8043248.
3 A. Thongtha, S. Maneewan, C. Punlek and Y. Ungkoon, *Energy Build.*, 2014, **84**, 516–525.
4 J. Li, Z. Wang, K. Zhang, C. Wang and X. Cui, *J. New Mater. Electrochem. Syst.*, 2019, **22**, 231–238.
5 X. Liang, C. Wang, J. Zhan, X. Cui and Z. Ren, *J. New Mater. Electrochem. Syst.*, 2019, **22**, 224–230.
6 Z. Wang, J. Li, P. Ye, C. Wang and X. Cui, *J. New Mater. Electrochem. Syst.*, 2020, **22**, 85–90.
7 F. Yang, X. Liang, Y. Zhu, C. Wang, G. Zhao and X. Cui, *J. New Mater. Electrochem. Syst.*, 2019, **22**, 159–164.
8 Y. Peng, Y. Liu, B. Zhan and G. Xu, *Constr. Build. Mater.*, 2021, **267**, 121792.
9 K. Matsui, J. Kikuma, M. Tsunashima, T. Ishikawa, S.-y. Matsuno, A. Ogawa and M. Sato, *Cem. Concr. Res.*, 2011, **41**, 510–519.
10 W. Qiankun, C. Youzhi, L. Fangxian, S. Tao and X. Bingbo, *J. Wuhan Univ. Technol.*, 2006, **21**, 17–20.
11 T. Mitsuda, K. Sasaki and H. Ishida, *J. Am. Ceram. Soc.*, 1992, **75**, 1858–1863.
12 L. Galvánková, J. Másilko, T. Solný and E. Štěpánková, *Procedia Eng.*, 2016, **151**, 100–107.
13 T. Shams, G. Schober, D. Heinz and S. Seifert, *Constr. Build. Mater.*, 2021, **287**, 123072.
14 M. Li, *J. Wuhan Univ. Technol.*, 2016, **31**, 1319–1322.
15 J. Jiang, X. Lu, T. Niu, Y. Hu, J. Wu, W. Cui, D. Zhao and Z. Ye, *Cem. Concr. Compos.*, 2022, **134**, 104734.
16 N. Milestone and G. Ahari, *Adv. Appl. Ceram.*, 2007, **106**, 302–308.
17 Y. Ungkoon, C. Sittipunt, P. Namprakai, W. Jetipattaranat, K.-S. Kim and T. Charinpanitkul, *J. Ind. Eng. Chem.*, 2007, **13**, 1103–1108.
18 N. H. H. G. Midgley, *Cem. Concr. Res.*, 1980, **10**, 213–221.
19 Z. Jing, F. Jin, T. Hashida, N. Yamasaki and H. Ishida, *J. Mater. Sci.*, 2007, **42**, 8236–8241.
20 C. Rios, C. Williams and M. Fullen, *Appl. Clay Sci.*, 2009, **43**, 228–237.
21 G. Smalakys and R. Siauciunas, *J. Therm. Anal. Calorim.*, 2018, **134**, 1–10.
22 X. Yang, C. Chong, X. Cui, G. Tang and H. Ma, *J. Wuhan Univ. Technol.*, 2014, **29**, 298–301.
23 Y. He, X. Zhao, L. Lu, L. Struble and S. Hu, *J. Wuhan Univ. Technol.*, 2011, **26**, 770–773.
24 S. Wang, X. Peng, L. Tang, L. Zeng and C. Lan, *Constr. Build. Mater.*, 2014, **60**, 42–47.
25 N. Mostafa, E. Kishar and S. Abo-El-Enein, *J. Alloys Compd.*, 2009, **473**, 538–542.
26 W. Mozgawa and M. Król, *J. Hazard. Mater.*, 2009, **168**, 1482–1489.
27 D. N. Saikia, P. Sengupta, P. K. Gogoi and P. Borthakur, *Cem. Concr. Res.*, 2002, **32**, 297–302.
28 S. Suzuki and E. Sinn, *J. Mater. Sci. Lett.*, 1993, **12**, 542–544.
29 Z. Wu, *J. Chin. Ceram. Soc.*, 1979, 262–270.